9

The Nature of Electromagnetic Waves in Metamaterials and Metamaterial-inspired Configurations

Rui Yang[1,2] and Yongjun Xie[1]
[1] *National Laboratory of Antennas and Microwave Technology, Xidian University, Xi'an, 710071,*
[2] *Department of Electronic Engineering Queen Mary College, University of London, London E1 4NS,*
[1]*China.*
[2]*UK*

1. Introduction

Metamaterials possessing various peculiar features have recently attracted an increasing amount of attention in the electromagnetics community. Their unexpected properties have opened up a number of different research directions that are geared towards the enhancement of the performance of microwave components, and overcoming current limitations. In this Chapter, the fundamental model properties of metamaterials and metamaterial based structures are demonstrated to study the renovated wave propagation.

2. Causality in the resonance behavior of metamaterials

Great of interest has been devoted to split ring resonator (SRR) which composes the essential part of left-handed materials [1-3]. Inherently bianisotropic, SRR metamaterials can be obtained by doping a host isotropic medium with two concentric rings separated by a gap, both having splits at opposite sides. As a result, besides the electric and magnetic coupling, the incident field also induces the magnetoelectric coupling [4,5]. Therefore, this kind of artificial magnetic media needs a careful control of the SRR orientation relative to the incident wave as well as the SRR design. Otherwise, the electromagnetic response is significantly more complicated. Smith et al. explored the electromagnetic characterization of the symmetric and asymmetric SRR plane [6]. Vasundara et al. presented the effects of gap orientation on the properties of SRR metamaterials with measured scattering parameters [7]. Aydin et al. investigated the influence of periodicity, misalignment, and disorder on the magnetic resonance gap of SRRs [8]. Gay-Balmaz et al. studied experimentally and numerically the electromagnetic resonances in individual and coupled SRRs [9]. Katsarakis et al. discovered the electric coupling to the magnetic resonance of SRRs under certain orientation [10]. Correspondingly, several analysis modals are employed to unravel the resonance property in the SRR transmission spectra, such as the physical intuition initiated by Pendry et al. [11], lumped element equivalent circuit model proposed by Martin et al.

Source: Wave Propagation in Materials for Modern Applications, Book edited by: Andrey Petrin,
ISBN 978-953-7619-65-7, pp. 526, January 2010, INTECH, Croatia, downloaded from SCIYO.COM

[12], and improved by Aznar et al. [13]. Meanwhile, lots of numerical simulations as well as experimental verifications are carried out for the metamaterial design [14-16]. Especially, Simovski et al. clarified the physical meaning of local constitutive parameters of metamaterials [17], and discussed Bloch material parameters of magneto-dielectric metamaterials [18].

A rigorous full wave analysis of bianisotropic SRR metamaterials is presented here for different electromagnetic field polarization and propagation directions. An alternative physical explanation is gained by revealing the fact that imaginary wave number leads to the SRR resonance. The field distribution over SRRs is then expanded into Floquet modes [19,20] to examine the transmission properties through metamaterials under arbitrary incident waves. Evanescent Floquet modes are proved to engender the resonance behavior which accords with the full wave analysis.

2.1 Full wave analysis of the SRR metamterials

To account for the magnetoelectric coupling in Maxwell's equations, SRR metamaterials can be described by the constitutive relations [21]

$$\boldsymbol{D} = \varepsilon_0(\bar{\varepsilon} \cdot \boldsymbol{E} + Z_0 \bar{\kappa} \cdot \boldsymbol{H}) \tag{1a}$$

$$\boldsymbol{B} = \mu_0(-\frac{1}{Z_0}\bar{\kappa}^T \cdot \boldsymbol{E} + \bar{\mu} \cdot \boldsymbol{H}) \tag{1b}$$

where $Z_0 = \sqrt{\mu_0/\varepsilon_0}$, $\bar{\varepsilon}$ and $\bar{\mu}$ are the relative electric permittivity and relative magnetic permeability tensors, $\bar{\kappa}$ is the magnetoelectric coupling dimensionless tensor.

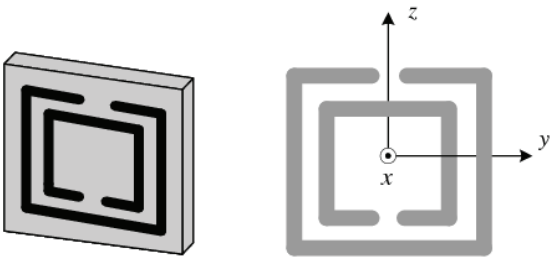

Fig. 1. The SRR unit cell

For axes fixed to the SRR as shown in Fig. 1, only certain components of $\bar{\varepsilon}$, $\bar{\mu}$ and $\bar{\kappa}$ tensors are of significance without losses [4,5]

$$\varepsilon_{xx} = 1,\ \varepsilon_{yy} = a + \frac{b\omega^2}{(\omega_0^2 - \omega^2)},\ \varepsilon_{zz} = a \tag{2a}$$

$$\mu_{xx} = 1 + \frac{c\omega^2}{(\omega_0^2 - \omega^2)},\ \mu_{yy} = 1,\ \mu_{zz} = 1 \tag{2b}$$

$$\kappa_{yx} = -i\kappa = -\frac{id\omega_0\omega}{(\omega_0^2 - \omega^2)} \tag{2c}$$

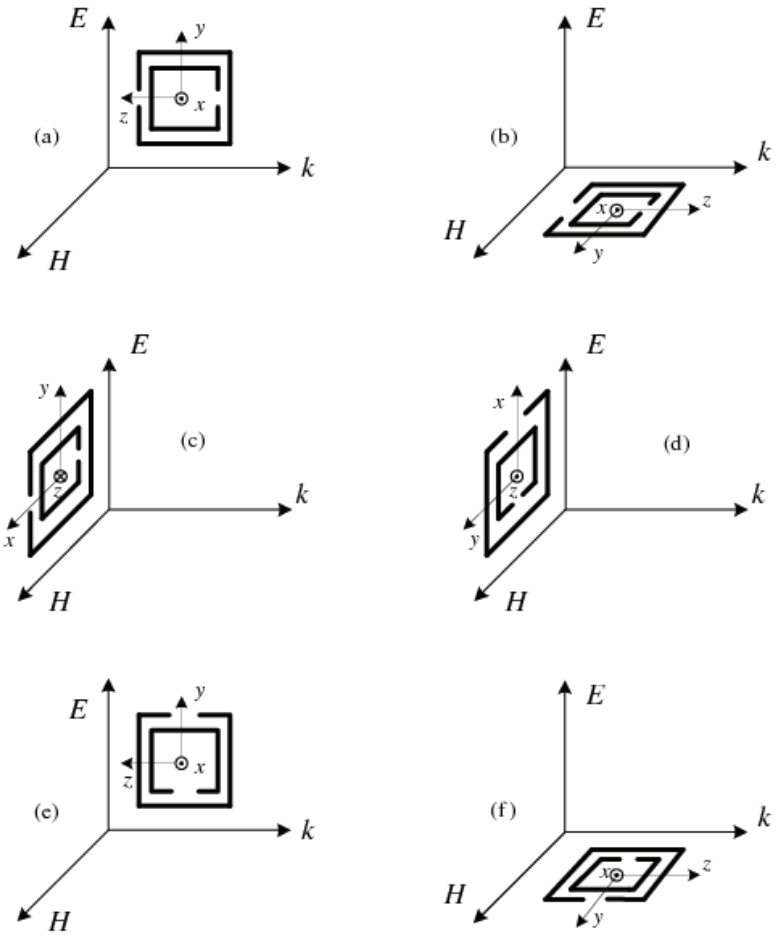

Fig. 2. Six orientations of SRR relative to different electromagnetic field polarization and propagation direction

ω_0 is the resonance frequency, and *a*, *b*, *c*, *d* in Fig. 1 are related to the geometry of the SRR. For other SRR orientations, the $\bar{\varepsilon}$, $\bar{\mu}$ and $\bar{\kappa}$ tensors just need a coordinates transformation. Introducing a normalized magnetic field $\boldsymbol{h} = Z_0 \boldsymbol{H}$, from Maxwell's curl equation for source free regions together with (1), (2), one may write

$$-\mathrm{i}\nabla' \times \mathbf{h} = \bar{\varepsilon} \cdot \mathbf{E} + \bar{\kappa} \cdot \mathbf{h} \tag{3a}$$

$$\mathrm{i}\nabla' \times \mathbf{E} = -\bar{\kappa}^T \cdot \mathbf{E} + \bar{\mu} \cdot \mathbf{h} \tag{3b}$$

where $\nabla' = \nabla / k_0$.

For the case in Fig. 2a, where magnetic field $\boldsymbol{H}$ is perpendicular to the SRR plane and incident $\boldsymbol{E}$ is parallel to the gapbearing sides of SRR. One obtains

$$(\kappa_{yx} + \beta)h_x = -\varepsilon_{yy}E_y \tag{4a}$$

$$(\kappa_{yx} - \beta)E_y = \mu_{xx}h_x \tag{4b}$$

The normalized wave number of the TEM wave satisfies

$$\beta^2 = \mu_{xx}\varepsilon_{yy} + \kappa_{yx}^2 \tag{5}$$

Ref. [4] concluded the same results by considering the bianisotropy role in SRR metamaterials. At given frequency ω, only those modes having $\mu_{xx}\varepsilon_{yy} + \kappa_{yx}^2 > 0$ will propagate. Those modes with $\mu_{xx}\varepsilon_{yy} + \kappa_{yx}^2 < 0$ will lead to an imaginary β, meaning that all field components will decay exponentially away from the source of excitation. Since $\kappa_{yx}^2 < 0$, this SRR orientation will achieve the resonance stop band when the constitutive parameters are single negative, including $\varepsilon_{yy} > 0$, $\mu_{xx} < 0$ case, as well as $\varepsilon_{yy} < 0$, $\mu_{xx} > 0$ case. When the constitutive parameters are double negative or double positive with the condition $\left|\mu_{xx}\varepsilon_{yy}\right| < \left|\kappa_{yx}^2\right|$, the resonance stop band will also occur.

For the case in Fig. 2b, where incident ***E*** is perpendicular to the SRR plane, and magnetic field ***H*** is parallel to the gapbearing sides of SRR, one obtains

$$\beta h_y = \varepsilon_{xx}E_x \tag{6a}$$

$$\beta E_x = \mu_{yy}h_y \tag{6b}$$

The normalized wave number satisfies

$$\beta^2 = \varepsilon_{xx}\mu_{yy} = 1 \tag{7}$$

which indicates that metamaterials with this SRR orientation has little influence to do with TEM waves of such electromagnetic field polarization and propagation direction. Meanwhile, there is no resonance stop band.

Through the similar analysis, metamaterials with the six SRR orientations can be re-categorized into three groups according to Maxwell's equations. The ones shown in Fig. 2a, 2b are one group, so do those in Fig. 2c, 2d, as well as those in Fig. 2e, 2f. The wave numbers for the other four cases are listed in Table 1. The case in Fig. 2c has been studied in Ref. [10],

SRR orientation	Fig. 2c	Fig. 2d	Fig. 2e	Fig. 2f
β^2	$\varepsilon_{yy}\mu_{xx}$	$\varepsilon_{xx}\mu_{yy}$	$\varepsilon_{yy}\mu_{xx}$	$\varepsilon_{xx}\mu_{yy}$
ε	$\varepsilon_{yy} = a + \dfrac{b\omega^2}{(\omega_0^2 - \omega^2)}$	$\varepsilon_{xx} = a$	$\varepsilon_{yy} = a$	$\varepsilon_{xx} = 1$
μ	$\mu_{xx} = 1$	$\mu_{yy} = 1$	$\mu_{xx} = 1 + \dfrac{c\omega_0^2}{(\omega_0^2 - \omega^2)}$	$\mu_{yy} = 1$

Table 1. Wave numbers for the SRR metamaterials shown in Fig2. c ~ Fig2. f.

where the authors identified the SRR with its outer ring at low frequencies, and illustrated the simulated currents to explain the resonance phenomenon. Here we can see it more clearly that ε_{yy} becomes less than zero when frequency ω is larger than the resonance frequency ω_0, leading to the imaginary wave number β, thus the resonance stop band is achieved. Also Fig. 2e case has the chance to become resonance when $\mu_{xx} < 0$, and there is no resonance stop band for the Fig. 2d and Fig. 2f case.

From the analysis above we can easily conclude that imaginary wave number actually leads to the SRR resonance. Such result has been noted by Simovski *et al.* in their previous work when studied the metamaterial parameters [17,18]. Here we provide an alternative means of characterizing the resonance of SRR metamaterials.

2.2 Floquet modes analysis of the SRR metamterials

Consider an electromagnetic wave to be incident on the SRR metamaterial plane with each element distributed periodically along $\hat{x}$ and $\hat{y}$ direction as shown in Fig. 3.

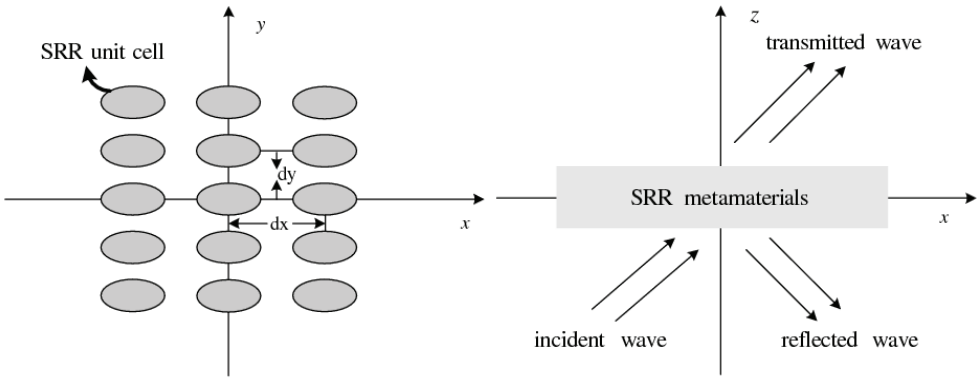

Fig. 3. Geometry of SRR metamterial plane with incident plane wave (a) Front view (b) Side view

The electromagnetic fields near the SRR elements must satisfy the periodicity requirements imposed by Floquet's theorem. Thus the scattered and the transmitted fields can be expanded as [20]

$$\boldsymbol{E}_{S(T)} = \sum_{m=1}^{2} \sum_{p=-\infty}^{+\infty} \sum_{q=-\infty}^{+\infty} R_{mpq}(B_{mpq}) \boldsymbol{\Psi}_{mpq} \tag{8}$$

where R_{mpq} and B_{mpq} stand for the reflection and the transmission coefficients respectively. The TE and TM vector mode functions $\boldsymbol{\psi}_{mpq}$ can be written as

$$\boldsymbol{\psi}_{1pq} = \frac{1}{(d_x d_y)^{1/2}} \left(\frac{v_{pq}}{t_{pq}} \hat{\boldsymbol{x}} - \frac{u_{pq}}{t_{pq}} \hat{\boldsymbol{y}} \right) \varphi_{pq} \qquad \text{TE-Floquet mode} \tag{9a}$$

$$\boldsymbol{\psi}_{2pq} = \frac{1}{(d_x d_y)^{1/2}}\left(\frac{u_{pq}}{t_{pq}}\hat{\boldsymbol{x}} + \frac{v_{pq}}{t_{pq}}\hat{\boldsymbol{y}}\right)\varphi_{pq} \qquad \text{TM-Floquet mode} \tag{9b}$$

The dominant modes have $p = q = 0$ and the higher order modes have $p \neq 0$ or $q \neq 0$. And

$$\varphi_{pq} = \exp(-i(u_{pq}\hat{\boldsymbol{x}} + v_{pq}\hat{\boldsymbol{y}} + \gamma_{pq}\hat{\boldsymbol{z}})) \tag{10}$$

Suppose the incidence wave in the direction of (θ, ϕ) with the wave number k, one has

$$u_{pq} = k\sin\theta\cos\phi + 2\pi p / d_x \tag{11a}$$

$$v_{pq} = k\sin\theta\sin\phi + 2\pi q / d_y \tag{11b}$$

$$\begin{aligned} \gamma_{pq} &= (k^2 - t_{pq}^2)^{1/2}, && \text{for } k^2 > t_{pq}^2 \\ &= -i\left|(k^2 - t_{pq}^2)^{1/2}\right| && \text{for } k^2 < t_{pq}^2 \end{aligned} \tag{11c}$$

with

$$t_{pq}^2 = u_{pq}^2 + v_{pq}^2 \tag{12}$$

It is known that a homogenous electromagnetic wave can always be decomposed into a combination of two plane waves with E-field perpendicular or parallel to the incident plane corresponding to the TE- and TM-Floquet modes. Therefore, the effects of any incident wave of either polarization at arbitrary angle (θ, ϕ) will be easily examined for the SRR resonance behavior.

The modal propagation constant γ_{pq} is positive real for the propagating modes and is negative imaginary for the evanescent modes. Since the resonance of SRR metamaterials is often manifested by a dip in the transmitted curves, let's see the *S* parameters for the SRR metamaterial plane.

$$S_{11}^{mpq} = \frac{R_{mpq}(1 - T_{pq}^2)}{1 - R_{mpq}^2 T_{pq}^2},\ S_{21}^{mpq} = \frac{T_{pq}(1 - R_{mpq}^2)}{1 - R_{mpq}^2 T_{pq}^2} \tag{13}$$

with the reflection coefficients $\left|R_{mpq}\right| \leq 1$ and propagation factor $T_{pq} = \exp(-\mathrm{i}\gamma_{pq} z)$. Apparently, S_{21} decreases while T_{pq} gets smaller. When γ_{pq} becomes pure imaginary, all the field components will decay exponentially from the source of excitation, leading to the dip in transmitted (S_{21}) curves. This reveals the fact that evanescent Floquet modes actually engender the resonance behavior which exactly accords with the full wave analysis.

Consider the SRR metamaterials with the orientation in Fig. 2a, the dimensions of the SRR defined in (2) are $a = 0.84$ mm, $b = 1.17$ mm, $c = d = 0.33$ mm, and the dielectric substrate with $\varepsilon_r = 4.8$ is 1.6 mm thick. The SRR metamaterial plane is 3.63 mm in $\hat{\boldsymbol{z}}$ direction with element period $dx = 5.6$ mm, $dy = 5$ mm along $\hat{\boldsymbol{x}}$ and $\hat{\boldsymbol{y}}$ direction. Fig. 4 shows the resonance behavior for a plane wave incident in the XoZ plane ($\phi = 0^\circ$). With E field perpendicular to the incident plane, the resonance only happens in the TE-Floquet modes.

The resonant frequency 8.2 GHz hardly changes, while the resonance intensity is sensitive to the incident angle. One knows that an H component perpendicular to the SRR plane will induce a circular current flow inside the SRRs, which in turn produces just above the resonance frequency a large magnetic dipole moment antiparallel to $H_{\perp} = H\cos\theta$, leading to a negative μ. As the SRR orientation shown in Fig. 2a, the E-field parallel to the gap bearing also introduces the electric resonance, thus the SRR resonance behavior becomes more complicated as the variation of incident angle. As shown in Fig. 4a, when $\theta = 40^{\circ}$, the resonance intensity is of most significance. When $\theta = 0^{\circ}$ and $\theta = 20^{\circ}$, one obtains the almost equal resonance intensity. When $\theta = 60^{\circ}$, the resonance is much weaker. In addition, the bandwidth increases a little as the incidence angle increases. The phases of S_{11} and S_{21} for the SRR metamaterials are given in Fig. 4b. When $\theta = 0^{\circ}$, one finds that the phase of S_{11} goes to zero and S_{21} has an extremely sharp change at the resonance point, which makes the metamaterials can be characterized as a magnetic conductor in this region. However, this does not hold true for the most significant resonance intensity when $\theta = 40^{\circ}$, since it is not merely engendered by H component.

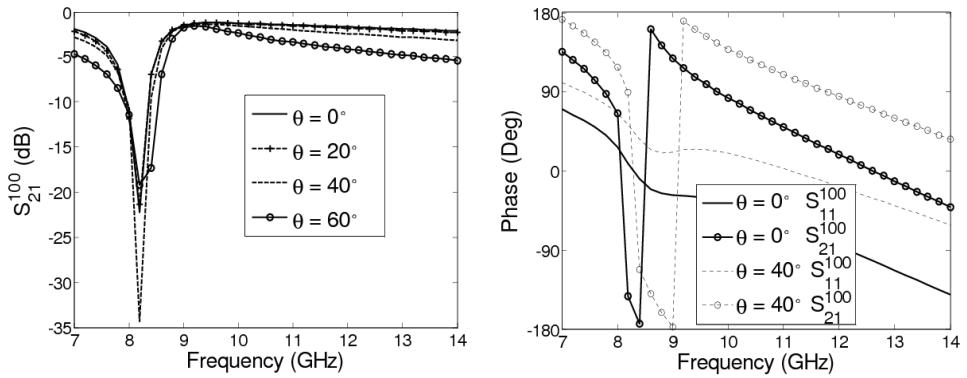

(a) (b)

Fig. 4. Transmitted TE-Floquet modes for the SRR metamaterials with the orientation in Fig. 2a (a) magnitudes (b) phases

The graph in Fig. 5 shows the resonance behavior for a plane wave incident in the YoZ plane ($\phi = 90^{\circ}$). With E-field parallel to the incident plane, the resonant behavior this time only happens in the TM-Floquet modes. Similar to the resonance behavior in Fig. 4a, the resonance frequency 8.2 GHz stays the same but the resonance intensity changes with the incidence angle. When $\theta = 60^{\circ}$, the resonance intensity is of most significance. When $\theta = 20^{\circ}$ and $\theta = 40^{\circ}$, one obtains the almost equal and weakest resonance. The intermediate resonance intensity is obtained when $\theta = 0^{\circ}$. The bandwidth decreases a little as the incidence angle increases. In Fig. 5b the phases of S parameters are illustrated. One finds that metamaterials can still be characterized as a magnetic conductor when $\theta = 0^{\circ}$, while the phase of S_{11} and S_{21} are more complex when $\theta = 60^{\circ}$.

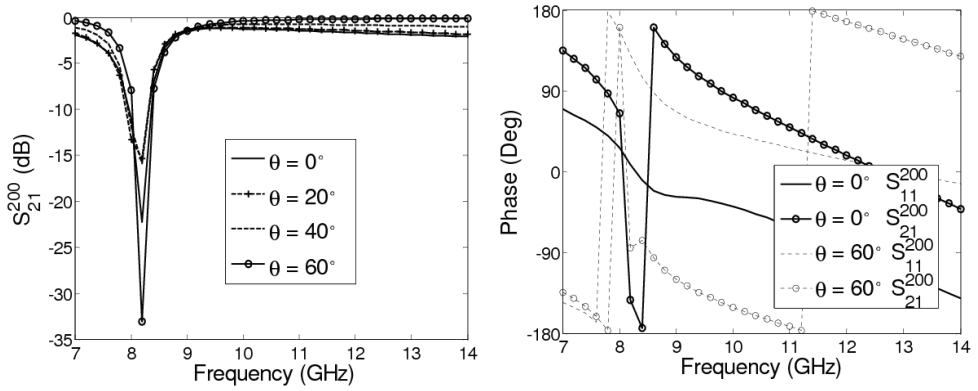

(a) (b)

Fig. 5. Transmitted TM-Floquet modes for the SRR metamaterials with the orientation in Fig. 2a (a) magnitudes (b) phases

Table 2 demonstrates the transmission factor for TE- and TM-Floquet modes at the resonance frequency 8.2 GHz . As is shown, $|T|$ turns smaller when the resonance intensity becomes more significant. And it is the fact that $|T|$ turns smaller because the evanescent modes play more important role, therefore one can conclude that metamaterial resonance is engendered by the evanescent Floquet modes.

TE-Floquet mode $\phi = 0^\circ$	$\theta = 0^\circ$	$S_{11}^{100} = -0.4117 + \mathrm{i}(-0.9080)$ $S_{21}^{100} = -0.0614 + \mathrm{i}(-0.0466)$	$\lvert T\rvert = 0.0424$
	$\theta = 40^\circ$	$S_{11}^{100} = 0.7535 + \mathrm{i}(-0.6571)$ $S_{21}^{100} = 0.0001 + \mathrm{i}(0.0193)$	$\lvert T\rvert = 0.0147$
TM-Floquet mode $\phi = 90^\circ$	$\theta = 0^\circ$	$S_{11}^{200} = -0.4117 + \mathrm{i}(-0.9080)$ $S_{21}^{200} = -0.0614 + \mathrm{i}(-0.0466)$	$\lvert T\rvert = 0.0424$
	$\theta = 60^\circ$	$S_{11}^{200} = 0.6596 + \mathrm{i}(-0.8780)$ $S_{21}^{200} = 0.0019 + \mathrm{i}(-0.0222)$	$\lvert T\rvert = 0.0126$

Table 2. Transmission factor for TE- and TM-Floquet modes at the resonance frequency 8.2 GHz

For the other two resonance cases in Fig. 2c (1.6 mm thick in $\hat{z}$ direction with $dx = 3.63$mm , $dy = 5$ mm) and Fig. 2e (5 mm thick in $\hat{z}$ direction with $dx = 5.6$ mm , $dy = 3.63$ mm), Fig. 6 shows the resonance behavior for a plane wave incident in the XoZ plane ($\phi = 0^\circ$) and similar results hold true for the wave incident in the YoZ plane ($\phi = 90^\circ$). The electric resonance for Fig. 2c case shown in Fig. 6a has the most significance resonance intensity when $\theta = 30^\circ$ at 8.6 GHz . On the other hand, the magnetic resonance for Fig. 2e case shown in Fig. 6b demonstrates the general downward trend with the incident angle 8.8 GHz , which has its most significant intensity when $\theta = 0^\circ$, and weakest when $\theta = 60^\circ$.

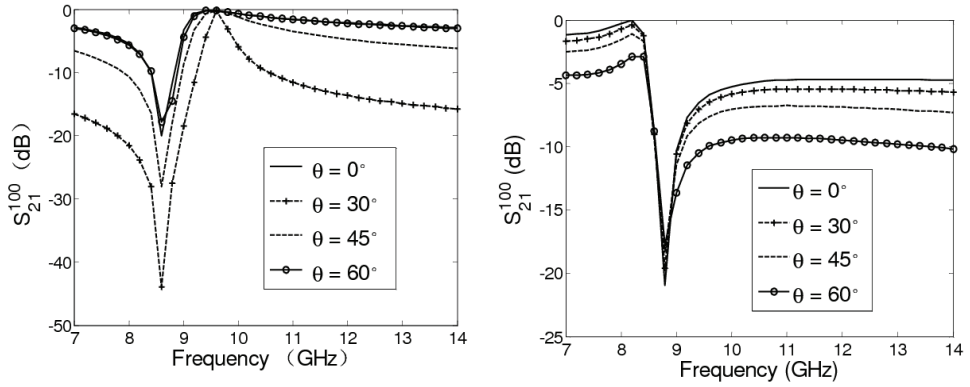

(a) (b)

Fig. 6. Transmitted TE-Floquet modes for the SRR metamaterials with (a) the orientation in Fig. 2c (b) the orientation in Fig. 2e

3. Propagation features of waveguides structures with SRR metamaterials

Waveguiding structures based on metamaterial media have recently been considered by several research groups showing how the presence of one or both negative constitutive parameters may give rise to unexpected and interesting propagation properties [22]-[29]. The absence of fundamental mode and sign-varying energy flux in the negative refractive index waveguide are revealed [25]. Rectangular waveguide filled with anisotropic single negative metamaterials are shown to support backward-wave propagation [26]. Moreover, Results for isotropic double negative metamaterial H waveguides are reported, including backward propagation, mode bifurcation and coupling effects [27]. The use of single negative metamaterials as the embedding medium for nonradiative dielectric (NRD) waveguides is examined [28]. Unimodal surface wave propagation in metamaterial NRD waveguides is obtained [29]. However, the presented literatures almost focus on the negative effects of both permittivity and permeability to the metamaterial based waveguides, whereas magnetoelectric coupling of the bianisotropic effects may lead to more dramatically unexpected features in the waveguiding structures.

With the consideration above, metamaterial loaded waveguiding structures are investigated to explore the different dispersion properties of guided waves. It is shown that transverse magnetic and transverse electric waves with non-cutoff frequency and enhanced bandwidth become into existence under certain circumstances in metamaterial parallel plate waveguide and rectangular waveguide. When doping uniaxial bianisotropic SRR metamaterials into NRD waveguides and H waveguides, both longitudinal-section magnetic (LSM) and longitudinal-section electric (LSE) waves are capable of propagating very slowly due to metamaterial bianisotropic effects. Particularly, some abnormal higher-order LSM and LSE modes with negative slope of the phase constant versus frequency may appear when metamaterials are double negative. Such modes will eventually lead to the leakage. Fortunately, for other modes, leakage can be reduced due to the magnetoelectric coupling. Particularly, when the metamaterials are of single negative parameters, leakage elimination can be achieved.

3.1 Parallel plate waveguides and rectangular waveguides

Geometry of parallel plate waveguide and rectangular waveguides filled with SRR metamaterials are shown in Fig. 7. The strip width W in Fig. 7(a) is assumed to be much greater than the separation l between the two plates, so that fringing fields and any x-variation can be ignored. And it is standard convention to have the longest side of the rectangular waveguide along the x -axis, so that $u > v$ in Fig. 7(b).

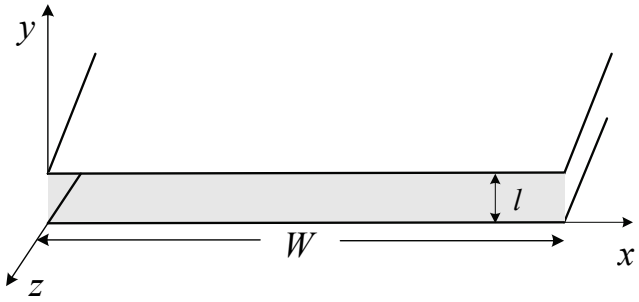

(a)

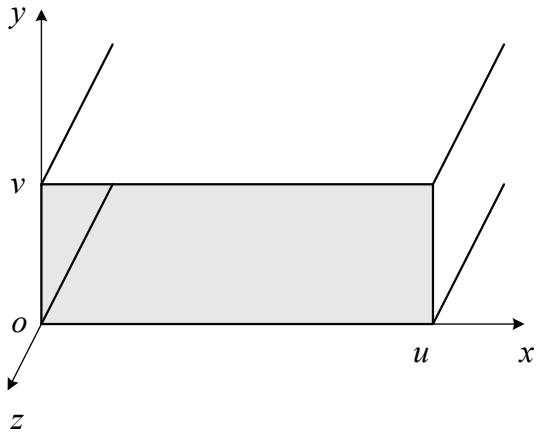

(b)

Fig. 7. Geometry of parallel plate waveguide and rectangular waveguide filled with SRR metamaterials

According to Fig. 2, metamaterial waveguide with different SRR orientations are illustrated in Fig. 8. For Fig. 8(a), one can express the following coupled equations for the longitudinal fields:

$$\begin{aligned}&\left(\frac{\varepsilon_{xx}}{\beta^2-\varepsilon_{xx}\mu_{yy}}\partial_{x'}^2+\frac{\varepsilon_{yy}}{\beta^2-\mu_{xx}\varepsilon_{yy}+\kappa^2}\partial_{y'}^2-\varepsilon_{zz}\right)E_z\\&\quad=\left(\frac{-\beta}{\beta^2-\varepsilon_{xx}\mu_{yy}}+\frac{\beta-i\kappa}{\beta^2-\mu_{xx}\varepsilon_{yy}+\kappa^2}\right)\partial_{x'y'}^2 h_z\end{aligned} \tag{14a}$$

$$\left(\frac{\mu_{xx}}{\beta^2-\mu_{xx}\varepsilon_{yy}+\kappa^2}\partial_{x'}^2+\frac{\mu_{yy}}{\beta^2-\varepsilon_{xx}\mu_{yy}}\partial_{y'}^2-\mu_{zz}\right)h_z = \left(\frac{-\beta}{\beta^2-\varepsilon_{xx}\mu_{yy}}+\frac{\beta-i\kappa}{\beta^2-\mu_{xx}\varepsilon_{yy}+\kappa^2}\right)\partial_{x'y'}^2 E_z \tag{14b}$$

3.1.1 Non-cutoff frequency modes

For the parallel plate waveguides, TM waves are characterized by $h_z = 0$ and a nonzero E_z field which satisfies the reduced wave Eq. (14a), with $\partial x' = 0$,

$$[\partial_{y'}^2+\frac{\varepsilon_{zz}}{\varepsilon_{yy}}(\mu_{xx}\varepsilon_{yy}-\kappa^2-\beta^2)]E_z = 0 \tag{15}$$

where

$$k_z^2 = \beta^2 k_0^2 = (\mu_{xx}\varepsilon_{yy}-\kappa^2)k_0^2-\frac{\varepsilon_{yy}}{\varepsilon_{zz}}k_c^2 \tag{16}$$

and $k_c = \frac{n\pi}{l}$, ($n = 0, 1, 2\cdots$) is the cutoff wave number constrained to discrete values.

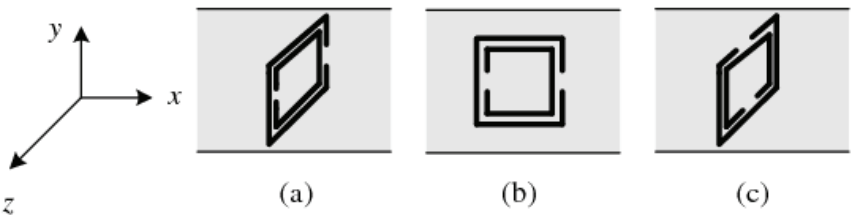

Fig. 8. Metamaterial waveguide with different SRR orientations

Observe that for $n = 0$, the TM_0 mode is actually identical to the TEM mode shown in Fig. 2(a), therefore, this TM_0 mode has a cutoff phenomenon while SRR resonance. However, from (16) one knows that TM mode has the chance to propagate with no cutoff frequency when $\varepsilon_{yy} < 0$ and $\mu_{xx}\varepsilon_{yy}-\kappa^2 > 0$, as shown in Fig. 9. Similar results hold true for the TE modes in Fig. 8(b), and TM modes in Fig. 8(c), which are corresponding to the resonance cases in the Fig. 2.

For the rectangular waveguides, one can see that if $\kappa \neq 0$, decoupling of E_z and h_z occurs only when $\partial_{x'} \equiv 0$ or $\partial_{y'} \equiv 0$, therefore we only consider TE_{mn} modes with $m = 0$ or $n = 0$, since neither m nor n can be zero for TM modes in a rectangular waveguide. When $\partial_{y'} \equiv 0$, one has the following decoupled equation and boundary condition for TE_{m0} modes from Eq. (14b)

$$(\partial_{x'}^2-\frac{\beta^2-\mu_{xx}\varepsilon_{yy}+\kappa^2}{\mu_{xx}}\mu_{zz})h_z = 0 \tag{17}$$

where

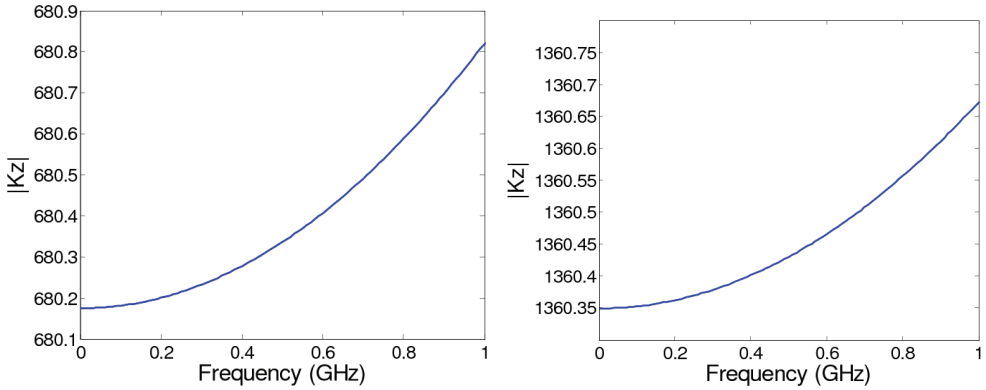

(a) TM_1 (b) TM_2

Fig. 9. The none cutoff frequency TM modes in parallel plate waveguide with SRR metamaterials $\varepsilon_{yy} = -3$, $\varepsilon_{zz} = 1$, $\mu_{xx} = -1$, $\kappa = 1$, $l = 8$ mm

$$k_z^2 = \beta^2 k_0^2 = (\mu_{xx}\varepsilon_{yy} - \kappa^2)k_0^2 - \frac{\mu_{xx}}{\mu_{zz}}k_c^2 \tag{18}$$

Akin to the modes in the parallel plate waveguide, none-cutoff frequency modes also exist under certain condition.

3.1.2 Enhanced bandwidth of single mode operation

For the parallel plate waveguides, the TE modes in Fig. 8(a), characterized by $E_z = 0$ and a nonzero h_z field which satisfies the reduced wave Eq. (14b), with $\partial x' = 0$. Through the similar derivation, one can obtain

$$f_c = \frac{nc}{2l} \qquad (n \geq 1) \tag{19}$$

The TM modes in Fig. 8(b), and TE modes in Fig. 8(c) corresponding to the non-resonance cases in the Fig. 2 achieve the identical cutoff frequencies $f_c = \frac{nc}{2l}$, which is the maximum value for ordinary TM and TE waves, promising a bandwidth enhancement for single-mode operation in material containing waveguide.

For the rectangular waveguides, one can see that TE_{0n} modes in Fig. 8(a) and Fig. 8(c) achieve the cutoff frequency of $f_c = \frac{nc}{2v}$, TE_{m0} modes in Fig. 8(b) obtains the cutoff frequency of $f_c = \frac{nc}{2u}$, which are equal to the ones of air containing rectangular waveguide, promising a bandwidth enhancement for single-mode operation in material containing waveguide.

3.2 Nonradiative dielectric waveguides and H waveguides

Consider the particular case of SRR metamaterials where two sets of SRR microstructures with different orientations are included in NRD waveguides and H waveguides as shown in Fig. 10.

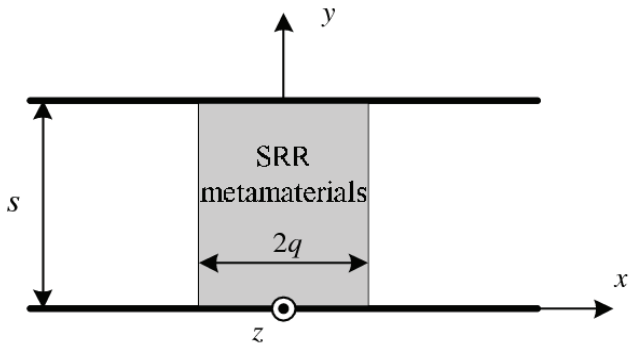

Fig. 10. Configuration of NRD waveguide and H waveguide with SRR metamaterials

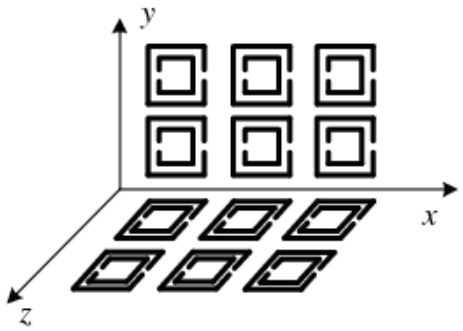

Fig. 11. Spatial orientation of SRRs in the host isotropic medium

The relative orientation of these two ensembles is in Fig. 11 and the $\bar{\varepsilon}$, $\bar{\mu}$ and $\bar{\kappa}$ tensors in Eq. (1) have the following uniaxial form [30]

$$\bar{\varepsilon} = \begin{bmatrix} \varepsilon_1 & 0 & 0 \\ 0 & \varepsilon_2 & 0 \\ 0 & 0 & \varepsilon_2 \end{bmatrix}, \bar{\mu} = \begin{bmatrix} \mu_1 & 0 & 0 \\ 0 & \mu_2 & 0 \\ 0 & 0 & \mu_2 \end{bmatrix}, \bar{\kappa} = \mathrm{i} \begin{bmatrix} 0 & 0 & 0 \\ 0 & 0 & \kappa \\ 0 & -\kappa & 0 \end{bmatrix} \tag{20}$$

where

$$\varepsilon_1 \propto a\,,\ \varepsilon_2 \propto 1 + \varsigma \frac{a(\omega_0^2 - \omega^2) + b\omega^2}{(\omega_0^2 - \omega^2)} \tag{21a}$$

$$\mu_1 \propto 1\,,\ \mu_2 \propto \xi + \frac{(\omega_0^2 - \omega^2) + c\omega^2}{(\omega_0^2 - \omega^2)} \tag{21b}$$

$$\kappa \propto \frac{d\omega_0\omega}{(\omega_0^2 - \omega^2)} \tag{21c}$$

ς , ξ reflect the different changes of ε and μ components in $\hat{y}\hat{y}$ and $\hat{z}\hat{z}$ direction. Therefore, ε_1 and μ_1 are always positive, whereas ε_2 and μ_2 can be negative in certain frequency band.

For the full wave analysis of the NRD waveguides and H waveguides modal properties, the eigenvalue problem is solved in the complex plane so as to examine the leakage property of H waveguides. The LSM modes are characterized by $h_x = 0$ with nonzero h_y as the supporting field which satisfies

$$\partial_{x'}^2 h_y + \frac{\varepsilon_2}{\varepsilon_1}\partial_{y'}^2 h_y = -(\varepsilon_2\mu_2 - \kappa^2 - \frac{\varepsilon_2}{\varepsilon_1}k_z^{'2})h_y \tag{22}$$

where $k_z^{'} = k_z/k_0 = \beta_z - \mathrm{i}\alpha_z$ is the complex normalized longitudinal wave number. All other field components can be expressed as

$$h_z = -\mathrm{i}\frac{1}{k_z^{'}}\partial_{y'}h_y \tag{23a}$$

$$E_x = -\frac{1}{k_z^{'}\varepsilon_1}(\partial_{y'}^2 h_y - k_z^{'2}h_y) \tag{23b}$$

$$E_y = \frac{1}{k_z^{'}\varepsilon_2}(\partial_{y'}\partial_{x'}h_y - \kappa\partial_{y'}h_y) \tag{23c}$$

$$E_z = -\mathrm{i}\frac{1}{\varepsilon_2}(\partial_{x'}h_y - \kappa h_y) \tag{23d}$$

Express h_y as a product of two separate variable functions in the form

$$h_y = f(x')g(y')\exp(-\mathrm{i}k_z^{'}z') \tag{24}$$

such that

$$\partial_{x'}^2 f(x') + k_x^{'2} f(x') = 0 \tag{25a}$$

$$\partial_{y'}^2 g(y') + k_y^{'2} g(y') = 0 \tag{25b}$$

where $k_x^{'} = k_x / k_0$ and $k_y^{'} = k_y / k_0$ are the complex normalized transverse wave numbers. Substituting back into Eq. (22), the normalized wave numbers can be expressed

$$k_{x1}^{'2} + \frac{\varepsilon_2}{\varepsilon_1}(k_y^{'2} + k_z^{'2}) = \varepsilon_2\mu_2 - \kappa^2 \tag{26a}$$

$$k_{x0}^{'2} + k_y^{'2} + k_z^{'2} = 1 \tag{26b}$$

One has $k_x^{'} = k_{x1}^{'} = \beta_{x1} - \mathrm{i}\alpha_{x1}$ for $|x'| < q'$, while for $|x'| > q'$, one should take $k_x^{'} = k_{x0}^{'} = \beta_{x0} - \mathrm{i}\alpha_{x0}$. Apply the boundary conditions on the perfectly electric conductor planes to other field components, one can write

$$g(y') = G\sin(k_y^{'}y') \qquad (n = 1, 2, 3, \cdots) \tag{27}$$

where G is the amplitude constant, and $k_y^{'} = n\frac{\pi}{s'}$ with $s' = k_0 s$. The n index gives the number of half waves along y. And

$$f(x') = \begin{cases} F_1 \exp[k_{x0}^{'}(x'+q')] & x' < -q' \\ F_2[\cos(k_{x1}^{'}x') + R\sin(k_{x1}^{'}x')] & -q' < x < q' \\ F_3 \exp[-k_{x0}^{'}(x'-q')] & q' < x' \end{cases} \tag{28}$$

Enforcing the continuity conditions at both $x' = \pm q'$, the modal equation for the LSM modes can be finally derived

$$[k_{x1}^{'}\cot(k_{x1}^{'}q') + k_{x0}^{'}\varepsilon_2][k_{x1}^{'}\tan(k_{x1}^{'}q') - k_{x0}^{'}\varepsilon_2] + \kappa^2 = 0 \tag{29}$$

the order of eigensolution of Eq. (29) gives the m index ($m = 0,1,2,\cdots$) appearing in LSM_{mn}. From the similar derivation, the LSE modes can be defined as

$$[k_{x1}^{'}\cot(k_{x1}^{'}q') + k_{x0}^{'}\mu_2][k_{x1}^{'}\tan(k_{x1}^{'}q') - k_{x0}^{'}\mu_2] + \kappa^2 = 0 \tag{30}$$

and the normalized transverse wavenumber in the slab should be given by

$$k_{x1}^{'\,2} + \frac{\mu_2}{\mu_1}(k_y^{'\,2} + k_z^{'\,2}) = \varepsilon_2\mu_2 - \kappa^2 \tag{31}$$

instead of Eq. (26a). Hereafter, we only consider the LSM modes, and the following results hold true for the LSE modes.

3.2.1 Slow wave propagation

Figure 12(a) presents the operational diagram for LSM modes, the real part of the longitudinal wave number $|\beta_z|$ decreases gradually as the magnetoelectric coupling turns larger in the case that ε_2 and μ_2 are of positive values. Maximum κ is achieved under the cutoff condition $k_z^{'} = 0$.

$$|\kappa_{\max}| = \sqrt{\varepsilon_2\mu_2 - \left|\frac{\varepsilon_2}{\varepsilon_1}\right| k_y^{'\,2} - k_{x1}^{'\,2}} \tag{32}$$

Since the guide wavelength defined as $\lambda_g = \frac{2\pi}{\beta_z}$ becomes smaller when longitudinal wave number increases, the corresponding phase velocity $v = T\lambda$ of the modes will be much slower. From Eq. (21), one can see that in the frequency that ω is far larger than the resonance frequency ω_0, both positive ε_2 and μ_2 as well as smaller absolute value of κ can be obtained, thus slow wave propagation will appear.

In Fig. 12(b), one can see that $|\beta_z|$ shows a general upward trend when the magnetoelectric coupling becomes significant in the case that ε_2 and μ_2 are both negative. Minimum value for κ with the cutoff condition $k_z^{'} = 0$ can be obtained,

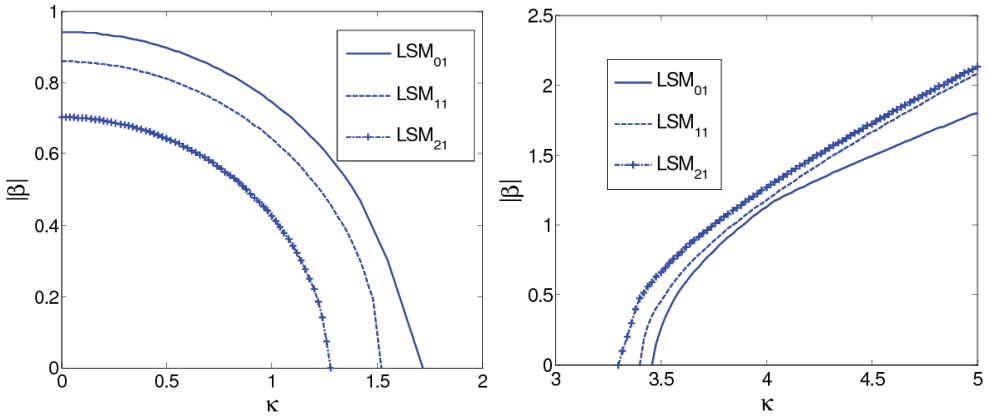

Fig. 12. Relationship of $|\beta_z|$ and magnetoelectric coupling κ in nonradiative dielectric waveguide with SRR metamaterials
(a) $\varepsilon_1 = 1$, $\varepsilon_2 = 3$, $\mu_2 = 2.5$, $f = 35$ GHz, $s = 0.4\lambda_0$, $q = 0.6\lambda_0$
(b) $\varepsilon_1 = 1$, $\varepsilon_2 = -3$, $\mu_2 = -2.5$, $f = 35$ GHz, $s = 0.4\lambda_0$, $q = 0.6\lambda_0$

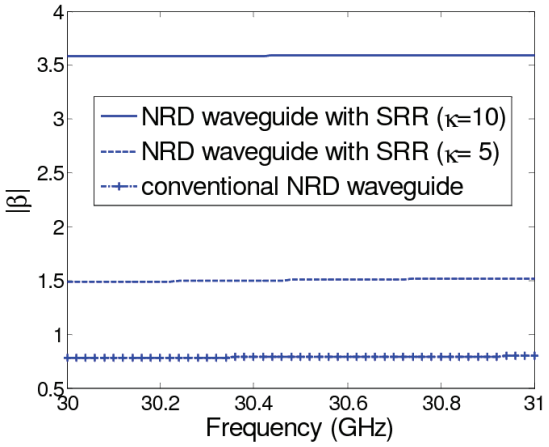

Fig. 13. Variation of the $|\beta_z|$ with frequency f for the dominant LSM_{01} (conventional NRD waveguide with $\varepsilon_r = 4$, $\mu_r = 1$, $s = 4$ mm, $q = 5$ mm ; double negative metamaterial NRD waveguide with $\varepsilon_1 = 1$, $\varepsilon_2 = -4$, $\mu_2 = -1$, $\kappa = 5$ and 10, $s = 4$ mm, $q = 5$ mm)

$$|\kappa_{\min}| = \sqrt{\varepsilon_2 \mu_2 + \left|\frac{\varepsilon_2}{\varepsilon_1}\right| k_y'^2 - k_{x1}'^2} \tag{33}$$

From Eq. (21), ε_2 and μ_2 have the chance to become negative when ω is little larger than the resonance frequency ω_0. Meanwhile, the magnetoelectric coupling κ has the absolute

value which can be infinitely large within this frequency band. Therefore, the guided waves are able to propagate very slowly, and even approach zero velocity.

Besides, we should stress that when the magnetoelectric coupling vanishes, Eq. (29) and Eq. (30) become a product of two elementary modal equations, which is similar to those of conventional NRD waveguides and H waveguides. Fig. 13 shows that the operational diagram for LSM_{01} modes in a conventional NRD waveguide and a NRD waveguide with SRR metamaterials. Since there exists minimum value for magnetoelectric coupling κ in the double negative case, we choose $\kappa = 5$ and 10 to make sure that LSM_{01} propagates. As can be seen within $[30\ \text{GHz},\ 31\ \text{GHz}]$, the longitudinal wave number of LSM_{01}mode in NRD waveguide with SRR metamaterials is always larger than that of the conventional one, thus traveling more slowly, which indicates that NRD waveguide with SRR metamaterials allows more number of wavelength to propagate within the same length, providing feasibility of miniaturization for NRD waveguide.

Let's further consider the power flow of LSM_{01} modes in the NRD waveguide with SRR metamaterials. The time-average power passing a transverse cross-section of the NRD waveguide is

$$\begin{aligned} P_{01} &= \frac{1}{2}\mathrm{Re}\int_{x'=-l'}^{l'}\int_{y'=0}^{s'} E\times h^{*}\cdot\hat{z}dy'dx' \\ &= \pm\frac{1}{2}\mathrm{Re}\int_{x'=-l'}^{l'}\int_{y'=0}^{s'} E_x h_y^{*}dy'dx' \\ &= \pm\frac{F_2^2G^2s'l'}{2\varepsilon_1}[\frac{1}{\beta_z}(\frac{\lambda_0}{2s})+\beta_z] \end{aligned} \tag{34}$$

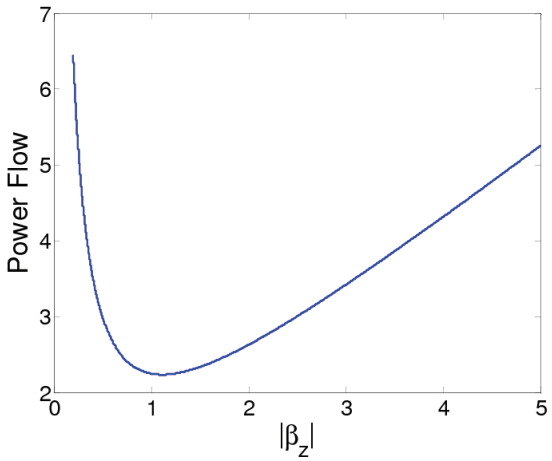

Fig. 14. Energy flow of LSM_{01} mode varied with longitudinal wave number in the NRD waveguide with SRR metamaterials

For ε_2 and μ_2 are both positive, we choose '+', and for the double negative metamaterial case, we choose '-'. As we all know, the double negative metamaterials have the negative wave number, which leads to the positive Poynting vector in Eq. (34). With the choice of